

Development of a multi-scale and coupled cutting model for the drilling of Ti-6Al-4V

Camille Bonnet, Thomas Pottier, Yann Landon

▶ **To cite this version:**

Camille Bonnet, Thomas Pottier, Yann Landon. Development of a multi-scale and coupled cutting model for the drilling of Ti-6Al-4V. CIRP Journal of Manufacturing Science and Technology, 2021, 35, pp.526-540. 10.1016/j.cirpj.2021.08.007 . hal-03337160

HAL Id: hal-03337160

https://imt-mines-albi.hal.science/hal-03337160

Submitted on 24 Sep 2021

HAL is a multi-disciplinary open access archive for the deposit and dissemination of scientific research documents, whether they are published or not. The documents may come from teaching and research institutions in France or abroad, or from public or private research centers.

L'archive ouverte pluridisciplinaire **HAL**, est destinée au dépôt et à la diffusion de documents scientifiques de niveau recherche, publiés ou non, émanant des établissements d'enseignement et de recherche français ou étrangers, des laboratoires publics ou privés.

Development of a multi-scale and coupled cutting model for the drilling of Ti-6Al-4V

Camille Bonnet[a,*], Thomas Pottier[a], Yann Landon[b]

[a] Institut Clément Ader (ICA), Université de Toulouse, CNRS, IMT Mines Albi, INSA, ISAE-SUPAERO, UPS, Campus Jarlard, Albi F-81013, France
[b] Institut Clément Ader (ICA), Université de Toulouse, CNRS, IMT Mines Albi, INSA, ISAE-SUPAERO, UPS, 3 rue Caroline Aigle, Toulouse 31400, France

Keywords:
Drilling
Numerical modeling
Ti-6Al-4V titanium alloy
Digital image correlation (DIC)
Infrared Thermography

A B S T R A C T

The present paper investigates the thermo-mechanical loading involved in hole drilling of Ti-6Al-4V. Indeed, the heat and strains developed in a very restricted area at the tool vicinity are responsible for various undesired side effects among which: tool damage, residual stresses, poor surface roughness, and metallurgical alterations. The confined nature of the drilling process prevents from any experimental access to some governing physical data such as local strain fields and local energies. Therefore a mixed numerical-experimental approach is herein proposed in order to provide local in-sight to essential tool-related thermal and mechanical sources. It relies on strain and temperature measurements at various locations of the cutting edge that are used to validate a multi-scale numerical model. This latter is then used to assess the energy budget involved in the material removal. The presented results prove the ability of such technique in obtaining valuable information on the in-process generated heat and the way it spreads within the workpiece and beyond. Results also show the spatial heterogeneity of the cutting phenomenon along the cutting edge and highlight the complexity of defining optimal cutting parameters and optimal tool design.

Introduction

In the aerospace industry, drilling is a common assembly process of titanium parts. However, this process generates high thermomechanical loadings in a very restricted area where heat builds up especially for low thermal conductivity materials such as titanium alloys. Ti-6Al-4V titanium alloy is widely used in the aerospace industry due to his relatively low density but is reputedly a hard-to-machine material [9]. The consequences of Ti-6Al-4V poor machinability are first the premature damage of drilling bits and second the part alterations in terms of roughness, microstructure or residual stresses. The purpose of this work is to provide quantitative information about amplitude, distribution and origin of the forces, heat and energies occurring in the drilling process.

For this purpose, a two folds approach is adopted. The first one relates to the use of experiments which enable to reveal these physical values at different scales. As the cutting area is difficult to access, the second part of the work deals with the development of numerical modelling to complete the initial investigations.

A large amount of physical values in machining, in particular in drilling, are determined by means of *post-mortem* investigations. For instance, Courbon et al. [12] use optical and scanning electron miscroscopes (SEM) to study microstructure and chip morphology in orthogonal cutting. Such means, along with investigations of the chip morphology are commonly employed in drilling [9,24]. X-ray diffraction (XRD) is also often chosen to determine the residual stresses. For example, Girinon et al. [18] realize XRD analyses on the walls of the drilled holes by cutting samples in two semi-cylinders. Micro-indent mapping is also used to assess the subsurface plasticity related hardening [58,17]. Other authors like Brynk et al. [7] choose to measure residual stress by means of digital image correlation (DIC) applied on external surface of drilled holes.

Global force measurements are also commonly performed by the mean of a dynamometer. The latter could be located under the workpiece or on the spindle [47,59]. Some authors [42,3] adopt a global-local approach to access local forces on the cutting edge during transient state. In the work of Poutord et al. [42], two edge discretization methods are compared. The first method consists of physically discretizing the cutting edge. Drilling tests on tubes and pin (or pre-holes) with various internal and external diameters are carried out and local efforts are determined by means of averaging. The principle of the second method is to discretize global efforts

* Corresponding author.
E-mail address: camille.bonnet@mines-albi.fr (C. Bonnet).

measured during transient state of drilling tests. Poutord et al. [42] underline that the second method is easier to set up compared to the first one for which a lot of samples and tests are required. In the work of Arif et al. [3], another comparison of these methods is presented. The authors notice that the numerical decomposition of the forces measured during the transient state led to an overestimation of forces compare to the other method. As a result, the authors conclude that the variation of the cutting edge geometry strongly influence the cutting forces.

The local temperature is very frequently evaluated at the cutting zone using thermocouples during drilling tests. Some authors choose to insert them within the tool, or in the lubrication holes [32,33].The heads of the thermocouples are tilted towards the cutting faces in the work of Le Coz et al. [33] and towards different areas of the cutting edge for Lazoglu et al. [32]. Besides, many authors perform pre-test drills around the investigated drill in order to insert several thermocouples close to the walls of the hole at different depths [14–16,21]. The other technique mainly used to evaluate the temperature during the drilling process is infrared thermography: point (pyrometry) or matrix (IR camera) information can be retrieved from such techniques. The use of pyrometry is generally based on the use of optical fibres (remote pyrometry). Lubrication holes can be used to insert the measurement point as close as possible to the cutting area [48]. Other authors choose to place the optical fibre in the workpiece in the axis of the tool to evaluate the temperature below the cutting edge [53,6]. In general, the optical fibre and the drill move synchronously to keep a constant distance between both and to avoid damages. Taskesen et al. [51] also choose to use synchronized optical pyrometer whose laser beam goes throught the tight hole to measure temperature below the cutting edge. The main disadvantage of such technologies (thermocouples and pyrometers) is that they provide punctual and/or averaged information. That is why many authors [56,40] use infrared thermography to evaluate thermal fields during the drilling process. Typically, drilling tests are carried out at the edge of the workpiece to observe the thermal fields close to the walls of the hole [13] in order to ease the use of inverse approaches [37,29] in solving the thermal equations.

The measurement of kinematic fields in machining tests is mainly based on post-processing methods of images obtained by high-speed camera. This post-processing can be carried out by several methods. The Particle Image Velocimetry approach [20,57] has been largely used but strain fields cannot be obtained in the case of an unstabilized cut. That is why other approaches have emerged more recently such as the use of grid methods [43] or Digital Image Correlation (DIC) [41,5]. It should be noted, however, that most of the work in this field focuses on a orthogonal cutting geometry, which is a simplification of a turning operation. In the case of the drilling process, this simplification is even further from the reality. In this respect, the work of Isobe et al. [26] propose a more applied approach. Indeed, they use photoelasticimetry method to determine the stress fields during an ultrasonic assisted drilling operation within a transparent acrylic resin.

In the present study, the reduced access to the cutting area is overcomed by means of drilling tests on tubes. Strain fields are determined by DIC with images obtained from high-speed camera. The thermal fields are measured using an infrared camera. Experimental thermomechanical fields are then compared with the drilling numerical model developed in the second part of the work in order to validate it. In the literature, machining processes are very regularly modelled by FEM, in particular the orthogonal cutting operation [22,25]. Li et al. [35] realize a 2D FEM orthogonal cutting model with a decreasing feed to model the milling process. In addition, it is interesting to note the work of Girinon [19] who develops an original 3D FEM model of the drilling process by means of two different model. The first ALE model represents matter flow and provides a thermal loading. This first model has the interest to avoid costly remeshing by using a mobile but rigid mesh of the drilled part. Following the application of the resulting thermal loading, residual stresses are deduced by means of a second model in Lagrangian formulation. In the litterature, Smoothed Particle Hydrodynamic approach (SPH) is an other notorious method to model machining process. This type of methods is based on interactions within a set of particles. It enables to avoid meshing and therefore mesh distorsion with large deformations. For instance, Calamaz et al. [8] develop a 2D SPH model to simulate the orthogonal cutting of Ti-6Al-4V. The authors underline that this model can highlight impact of tool wear on cutting forces and feed forces.

Many recent research works have focus on a more macroscopic scale. In such works, the elements deletion is often not modelled as such and the hole walls are simply loaded with a given thermo-mechanical distribution [54]. This popular approach, although a simplification of a far more complex underlying physics, has proven help-full in assessing the residual stresses generated along the tool path and various complementary studies have tried to link such mechanical footprint of the manufacturing process to the in-service fatigue resistance [38,30]. The major inconvenient that arises from this scale-up simplifications relies in the assessment of the thermo-mechanical loading in terms of amplitude, time dependence and above all the surface on which this loading should be applied.

The aim of the present study is therefore to propose a way of assessing the major features of this thermo-mechanical loading involved in the drilling of Ti-6Al-4V.

For this purpose, a local-global approach is adopted in this paper. The numerical model of the drilling process developed consists on the one hand of a 3D finite element modeling (FEM) implemented on ABAQUS/CAE [1] in a local scale and on the other hand of an 2D finite differences model (FDM) extended in time in a global scale. Thus, quantitative information brought by the two parts of the work makes enable the characterization and modelling of the cut phenomenon along the cutting edge during the drilling process at micrometric and millimetric scales.

Experimental set-up

Drilling tests

Drilling tests in dry conditions are carried out on a DMG DMU85eVo machine tool using fixed samples and a rotating drill configuration. Every test is repeated three times (in order to check repeatability of tests) and realized with a spindle speed of 450 rev/min and a feed rate of 0.1 mm/rev. These cutting conditions lead to a local cutting speed at the tool periphery around 15 m/min. They were chosen in the range of industrial cutting conditions and allow measurements at limited acquisition frequencies. The tool is manufactured by SECO (SD203A-11.0-33-12R1-M) and consists of a TiAlN coated cemented carbide twist drill with 11*mm* diameter (see parameters Fig. 1).

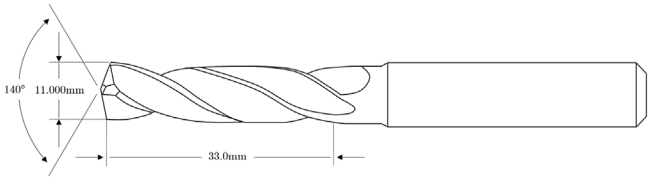


Fig. 1. Schematization of the SECO-SD203A-11.0-33-12R1-M twist drill [61] used in the experiment and several parameters: point angle, cutting diameter and usable length.

The cutting edges of the tool exhibit a complex geometry and is actually composed of several edge sections with different and changing rake angles (see red edge in Fig. 2 and γ_f evolution depicted in Fig. 3). Faced with the complex cutting edge geometry, an approach by edge discretization has been chosen.

Workpieces

In order to carry out this study by edge discretization and to overcome the difficulty of access to the cutting area, the drilling tests are realized on speckled tubes (or pin). Accordingly, the studied workpieces are three tubes and one pin made from forged Ti-6Al-4V with different sizes listed in Table 1. Studying the cut of these tubes of different diameters means looking at the cutting phenomena in different areas of the cutting edge, in other words in different cutting conditions (see Zones 1, 2, 3 and 4 in Fig. 4). For this spindle speed of 450*rev*/*min*, the local cutting speed V_c at the center of the thickness of each tube is listed in Table 1.

The influence of the distance from the axis of rotation on the cutting mechanisms can then be highlighted and quantified.

Instrumentation

In order to determine the *in-situ* strains and temperature fields at the cutting area of each sample, fast and infrared camera are instrumented (see Fig. 4). The chosen integration frequency and integration time are respectively 6000 Hz–1/6000 s and 600 Hz–100 µs with a [5.0230–5.119] µm band pass filter. The high speed camera is a Photron FASTCAM SA3 and the chosen infrared is a Mid-Wave FLIR SC7000 on which a so-called G1 lens is mounted. The visible image resolution is 512×512 and the infrared image resolution is 128×160. Examples of images obtained during experiments using these cameras are shown in Fig. 5.

The integration times of the two imaging device are chosen in order to prevent from motion blur while maintaining a sufficient amount of incoming flux to preserve from a detrimental signal-to-noise ratio.

Experimental considerations

Metric calibration

For both imaging apparatus, the knowledge of the metric size of the pixel is a key factor to any metroligical approach. Indeed, the high-speed camera is equipped with a tunable Infinity^{TM}-K2 microscope. In order to compare the obtained fields at the same location than the numerical results it is necessary to assess the exact magnification of the overall involved optics. Similarly, the exact magnification of the G1 germanium lens is not accurately known.

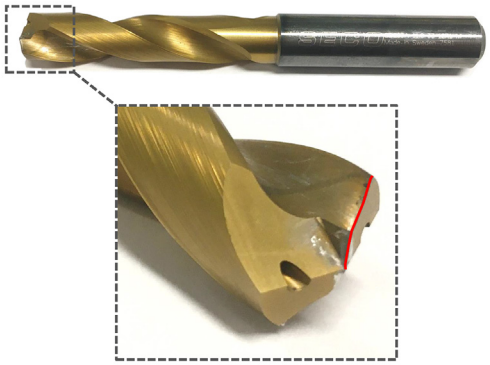


Fig. 2. SECO-SD203A-11.0-33-12R1-M twist drill used in the experiment.

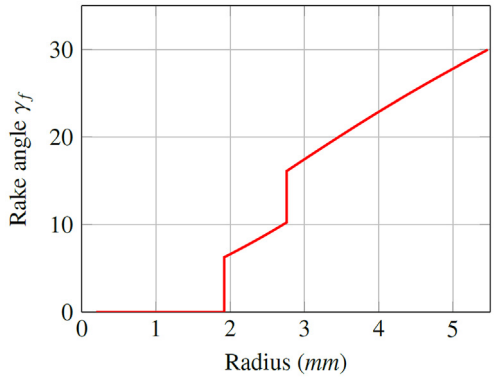


Fig. 3. Rake angle γ_f along the cutting edge of the SECO-SD203A-11.0-33-12R1-M ∅11 twist drill.

Table 1
Samples dimensions and local cutting speed V_c in the thickness of each sample.

	$\emptyset_{ext}$ (mm)	$\emptyset_{int}$ (mm)	Thickness (mm)	local V_c (m/min)
Tube T1	11.0	7.9	1.55	13.36
Tube T2	9.8	6.9	1.45	11.80
Tube T3	8.6	5.6	1.50	10.04
Pin P	5.6	–	–	3.96

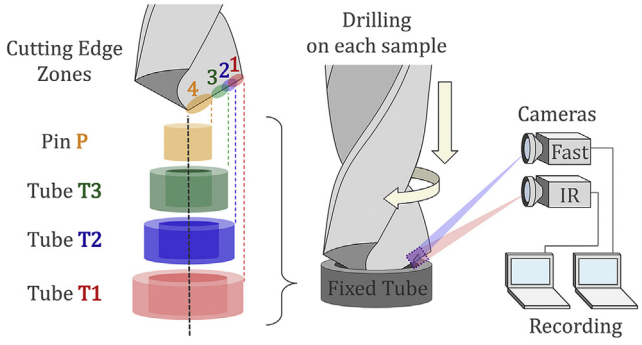


Fig. 4. Experimental set-up consisting of in-situ imaging of tube/pin drilling in the visible and infrared spectrum.

Accordingly, a simple magnification assessment has been setup using a Ronchi ruling targets at 12.5l pm and 5l pm respectively. The obtained images are depicted in Fig. 6 and enable the assessment of the metric size of the pixel from a straight-forward Fourrier transform. The calculated size are 3.692 µm/pix for the visible image and 47.958 µm/pix for the IR image.

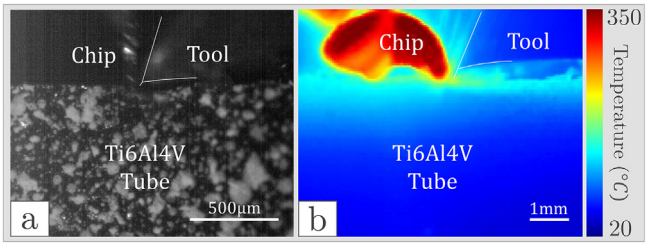
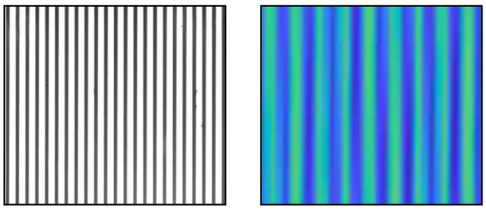


Fig. 5. Example of images obtained with fast (a) and IR (b) cameras – Tube T2.



a) Visible: 12.5 lpm b) IR: 5 lpm

Fig. 6. Images of the Ronchi targets used for visible (a) and IR (b) metric calibrations.

DIC

For all tests, local correlation scheme was used [49]. The subset size is set to 16×16 *pixels*. The quality of the imaged speckle is quantified through the computation of their respective Mean Intensity Gradient (MIG) [39]. Such approach allows to assess the expected standard deviation σ_u of the displacements for a given subset size. The MIG and σ_u values are summarized in Table 2.

Thermal calibration

The Infrared camera wavelength range is [2.5–5.5] μm. It therefore requires to paid attention to two factors

Emissivity – The emissivity of the black and white paints needed to perform digital image correlation which has been measured by the mean of a commercial IRTF spectrometer Brüker Vertex 70. The integrated emissivity over the specified wavelength range was assessed at 0.93 and 0.69 for the black a white paints respectively. It is worth noticing that the IR pixels size is way larger that the speckle pattern characteristic size. Accordingly, the black and white speckle is seen as "grey" (averaged) from the IR camera stand point. Consequently it has been assumed that the overall emissivity is the weighted average of the two aforementioned emissivities and reads 0.88.

Black-body calibration – A cavity black body has been used to obtain the radiometric curve. Optics, filter, integration time and focus was set the same as the real experiment. A total of 16 points ranging from 20° to 300° were captured. The complete radiometric curved were then reconstructed using piecewise polynomial interpolation.

Finally, a two-point non-uniformity correction has been addressed prior to the testings.

Table 2
Mean Intensity Gradient and expected standard deviation over the displacement u of the four investigated speckles.

	P	T3	T2	T1
MIG [GL/pix][a]	14.8	14.2	14.0	13.4
σ_u [pix]	0.025	0.085	0.080	0.086

[a] *GL* stands for Grey Levels, here coded over 256 GL (i.e. 8 bits).

Additional thermographic investigations

Performing Mid wave infrared thermography at small scale is known to trigger the so-called Size of Source Effect (SSE) [31,55]. The SSE is the ratio between the radiometric reading of an image exhibiting a handful of *hot* pixels within a *cold* image and the reading of the same pixels when a larger *hot* source is imaged. Indeed, when the size of the source increases, parasitic radiations enter the aperture of the camera and create scatters and reflections within the optics [60]. A correcting factor denoted *SSE* is therefore implemented to correct the intensity I read by the sensor. It depends on the amount of *hot* pixels within a given image i.

$$SSE_i(a) = \frac{I_i(a)}{I(a_{bb})} \tag{1}$$

where $I_i(a)$ is the direct reading of the sensor and a is the dimensionless aperture, defined as the ratio of *hot* pixels to the total number of pixels (128×160). A *hot* pixel is defined as exhibiting a digital level above the average of the dynamic range of the image (i.e. above $I_{min} + (I_{max} - I_{min})/2$). a_{bb} is the aperture used for black-body calibration, hence $I(a_{bb})$ is the actual correct reading of the temperature. As shown in Fig. 7, a simple experiment, performed with a tunable aperture placed in front of a cavity black-body set at 300°C, shows that the reading of the pixels at the center of the image vary as the number of *hot* pixels in the image increases (as the aperture size increases).

In the present work, the obtained images typically overlap this definition since a hot chip comes and goes within the image as the drill cuts. Accordingly, for each image, the digital level histogram is used to assess the amount of hot and cold pixels a. Then, the function depicted in Fig. 7 is used to assess the corresponding SSE, finally the thermal image is corrected numerically.

Finally, even if the InSb sensor is thermally regulated (Stirling refrigerator), the camera warm-up throughout experiment leads to increase the temperature of the casing and the optics and thus impairing the reading of digital levels. It is observed that such thermal drift is significant during the first two hours (from $T(t)/T_{stab} = 5.6\%$ error at $t = 0$ min to 1.2% at $t = 120$ min). After 120 min the reading stabilizes and slowly evolves to steady state T_{stab}. Accordingly, every experiment was performed after a two hours warm up time.

Drilling model

Thermomechanical model

Behaviour law and damage model

The material constitutive behaviour of the chosen material (see Eq. (2)) is the one used in the work of Harzallah et al. [22]. Under

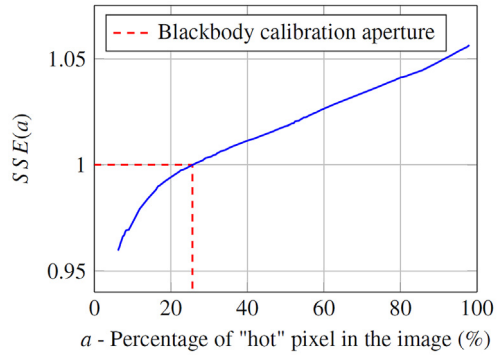


Fig. 7. Evolution of the size of source effect as a function of the dimensionless aperture a.

such formalism, the stress σ depends on coefficients A, B and n which correspond respectively to the yield strength, the strain-hardening modulus and the strain-hardening exponent and are set to be depending on both the strain-rate and the temperature.

$$\sigma = A(\dot{\varepsilon}, T) + B(\dot{\varepsilon}, T).\varepsilon_p{}^{n(\dot{\varepsilon},T)} \tag{2}$$

A, B and n are evaluated by means of the following equation of plane: $A, B, n = -a.T - b.\ln(\dot{\varepsilon}) - c$ where the parameters a, b and c are identified by Harzallah et al. [22] (see Table 3).

Damage is implemented through a classical D internal variable formulation [1]. Its value at $t + \Delta t$ is calculated from its value at the previous increment t, the plastic strain increment $\Delta\varepsilon_p$ and the equivalent strain at failure $\overline{\varepsilon_f}$ (See (3)).

$$D(t + \Delta t) = D(t) + \int_t^{t+\Delta t} \frac{\Delta\varepsilon_p}{\overline{\varepsilon_f}} \tag{3}$$

For each increment, the equivalent plastic strain at failure $\overline{\varepsilon_f}$ is evaluated for each integration point. This equivalent strain at failure ε_f is also defined according to the work of Harzallah et al. [22] and reads:

$$\overline{\varepsilon_f} = \left[\frac{\sqrt{3}.\tau_f(\dot{\varepsilon}, T)}{B(\dot{\varepsilon}, T) \quad \cos\left(\frac{\pi\overline{\theta}}{6}\right)} - \frac{A(\dot{\varepsilon}, T)}{B(\dot{\varepsilon}, T)} \right]^{\frac{-1}{n(\dot{\varepsilon},T)}} \tag{4}$$

Thus, the element deletion is triggered when the damage D (initially equal to zero, indicating an undamaged state) reaches the value 1 which corresponds to an extremely damaged state.

The damage onset yield $\overline{\varepsilon_f}$ results from an adaptation of the Mohr-Coulomb criterion with the proposed flow rule (see Eq. (2)). The strain at failure $\overline{\varepsilon_f}$ also depends on A, B and n as well as on the normalised Lode angle $\overline{\theta}$ and the maximum shear stress τ_f. The values of the material parameters A, B, n and τ_f for ranges of strain rates $\dot{\varepsilon}$ and temperatures T have been experimentally identified by Harzallah et al. [22]. This formulation enables to obtain an explicit coupling of the thermomechanical behaviour without the addition of multiplicative terms [27,8]. The material behavior can then be characterized without prejudging an evolution model of the strain-hardening or damage with respect to T and $\dot{\varepsilon}$.

The relevance of this formulation in the case of orthogonal cutting has been validated previously [22,23]. The choice of this formulation was therefore also guided by the idea of verifying if it is possible to extend the field of application of this formulation to the case of drilling of Ti-6Al4V.

Friction law

The friction law used in this paper combines the Coulomb-Orowan friction law and the Tresca law. The Coulomb-Orowan model enables to describe the stick-slip phenomenon observed in machining process [11]. Machining contact pressures are of the order of twice the flow stress of the most ductile material $\sigma_0/\sqrt{3}$ [50]. As long as the frictionally induced stress τ remains below this shear flow stress, the friction conditions correspond to a sticking contact. Above this value, the contact slides. In such case, the Tresca models defines the interfacial shear stress as a fraction (denoted m) of the yield shear stress $\sigma_0/\sqrt{3}$. The numerical friction behavior can be summarized as follows (Fig. 8):

Table 3
Parameters values for the Ti-6Al-4V behaviour law implemented in the FE model.

	A (mm)	B (mm)	C (mm)
a	$9.36e+005$	$5.57e+05$	$9.46e-05$
b	$-1.45e+08$	$4.66e+07$	$4.23e-02$
c	$-8.65e+08$	$-6.39+08$	-0.365

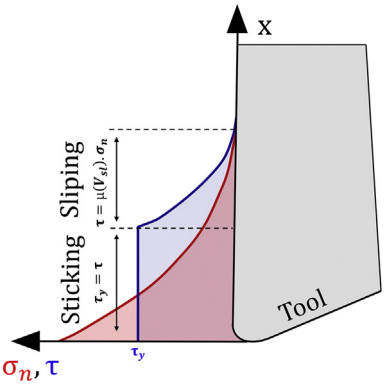


Fig. 8. Schematic representation of the friction model implemented on the rake and relief faces [22,44].

$$\begin{cases} \vec{\tau} = -\mu\sigma_n \dfrac{\vec{v_g}}{||\vec{v_g}||} & \text{if } ||\tau|| < \dfrac{\sigma_0}{\sqrt{3}} \\ \vec{\tau} = -m\dfrac{\sigma_0}{\sqrt{3}} \dfrac{\vec{v_g}}{||\vec{v_g}||} & \text{if } ||\tau|| = \dfrac{\sigma_0}{\sqrt{3}} \end{cases} \tag{5}$$

With respect to Harzallah's work [22], the friction coefficient μ is set to decrease with the cutting speed. The evolution of this coefficient is obtained via experimental results of Rech et al. [44].

Finite element model

For each sample, a Lagrangian 3D numerical model has been developed by means of ABAQUS/Dynamic Temp-disp Explicit [1] using 3D continuum elements under reduced integration (C3D8RT) with refined meshing in the cutting zone (500 μm to 4.5 μm). Fig. 9 shows models for the tube T1, the tube T2, the tube T3 and the pin P. In order to simplify the modeling, the tool axial motion is not considered (the undeformed mesh exhibits a conical top surface) and the implemented tool geometry is an approximation of the real tool geometry. The pin model is investigated over a 1/4 revolution while the tubes models are computed over a 1/8 revolution following a first pass of the drill. For every sample, the edge radius is 10 μm and a thermo-elastic behavior is assumed for the tool. In addition, a 500 μm radius area is removed on the center of the pin to exclude the complex phenomena that take place there. Besides, there is no heat exchange tool/workpiece and workpiece/air implemented in these models.

The chosen cutting conditions are the same as those used experimentally. Unlike many models presented in the literature, the present work deals with 3D models and does not seek help of a so-called sacrificial zone [36]. Consequently, both the behaviour and damage equations presented in the above are applied to the entire volume of the workpiece. Finally, the implementation of a such complex model inevitably requires the use of a material used subroutine VUMAT and a friction user subroutine VFRIC (Table 4).

Thermal aspect

The heat generated during the cutting process stems from two sources namely friction and plasticity. Concerning friction, the heat is implemented as follows

$$q_f = \eta\tau V_s \tag{6}$$

where τ is the frictional stress, V_s the slip velocity and η the ratio of frictional power converted into heat. This latter is routinely set to 0.9 [22]. This heat input is seen from the workpiece point of view as a surface flux entering the material through the top free surface.

Plasticity related heat generation is implemented through the Taylor-Quinney Coefficient β_{TQ} [52,45]. It is defined here under its differential form as the ratio of the calorific power to the anelastic

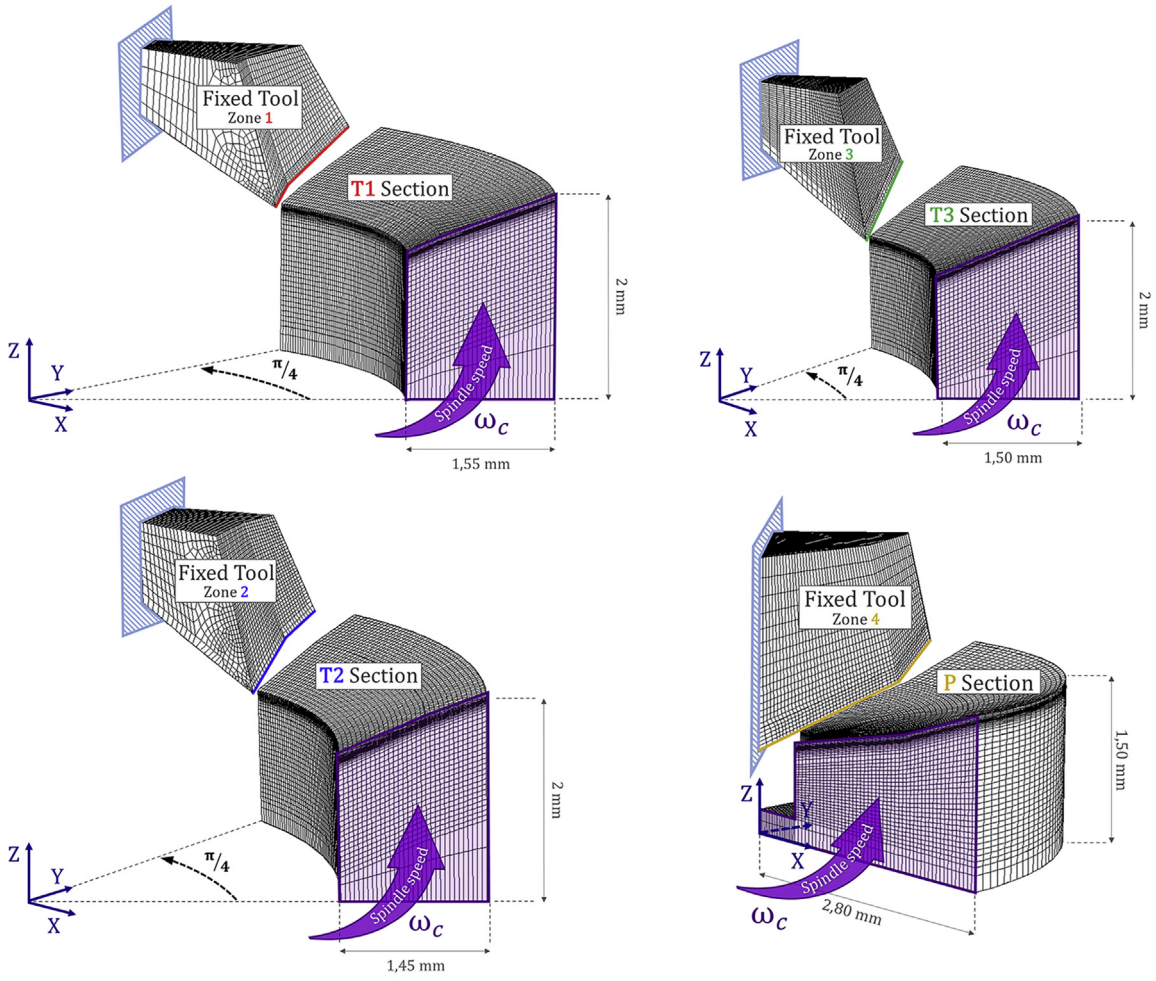


Fig. 9. FEM models.

Table 4
Numerical parameters (FEM).

Material properties	Workpieces	Tools
Density ρ (kg.m^{-3})	4430	15,900
Thermal conductivity λ (W.m^{-1}.K^{-1})	6.6	24
Specific heat C_p (J.kg^{-1}.K)	670	238
Young Modulus E (GPa)	113.39	70,500
Poisson coefficient ν	0.342	0.23
Ambient temperature T_{amb} (K)	293	–

power:

$$\beta_{TQ} = \frac{\rho C_p \Delta T}{\int \mathrm{d}w_p} \tag{7}$$

where ΔT is the temperature rise, C_p the specific heat, ρ the mass density and $\int \mathrm{d}w_p$ the specific anelastic work defined as a function of the stress to strain-rate contracted product:

$$\int \mathrm{d}w_p = \int \sigma : \dot{\varepsilon}_p \tag{8}$$

The dependency of β_{TQ} to the plastic strain has also been implemented. Indeed, according to the work of Rittel et al. [46] performed on the same material, in the same range of strain rate, and on shear/compression specimen, β_{TQ} evolves as the plasticity progresses toward the onset of fracture. For implementation purpose the dependency to the plastic strain is replaced by an evolution with the damage variable $D = \int d\varepsilon_p/\varepsilon_f$, where ε_f is the strain at failure defined in Eq. (4). As depicted in Fig. 10, the β_{TQ} evolution changes drastically when the damage variable becomes larger than 0.8. It has been approximated by a two linear regression defined as follows.

$$\beta_{TQ} = \begin{cases} a_0 D + b_0 & \text{if } D \leq 0.8 \\ a_1 D + b_1 & \text{if } D > 0.8 \end{cases} \tag{9}$$

where $a_0 = -0.22$, $b_0 = 0.54$, $a_1 = 3.2$ and $b_1 = -2.2$ are the regression parameters. Under such formalism the Taylor-Quinney coefficient

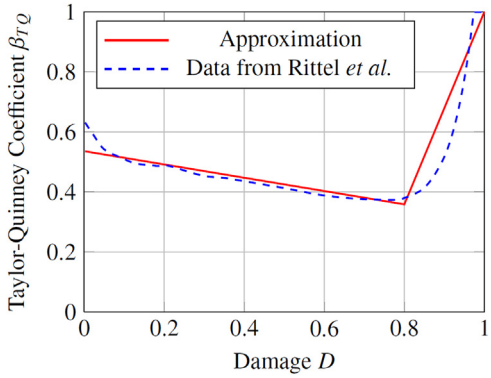


Fig. 10. Simplified linear model of the Taylor Quinney coefficient evolution over the damage range. Rittel et al. [46] experimental data superposed.

β_{TQ} explicitly depends to the state variable and can thus being implemented straight forwardly.

Extended thermal model

Finite element simulation of tube drilling over several turns requires the resolution of the explicit coupled models presented Fig. 9 over a considerable cut distance. This approach is in practice numerically very heavy and its stability over such a long cutting time leads to major difficulties. The results of the above models (over 1/4 or 1/8th of a turn) were therefore extended over 5 and 20 turns using a strictly thermal model. In order to develop a model which enables the progressive element deletion (and thus able to evacuate heat through the chip), a 2D finite difference (FDM) approach was implemented [2] (see Fig. 11). All free surfaces are submitted to convection and radiation conditions ($h = 50\,\mathrm{W.m^{-2}.K^{-1}}$ and $\varepsilon = 0.9$). As the model is 2D axisymetric, the simulated tube has only one element according to e_r with thickness e. The surface temperature is approximated to the mean through-thickness temperature which enables to estimate the term in $\partial^2/\partial r^2$ by a thermal leakage term [10]. Under such an hypothesis, the two-dimensional heat diffusion equation is established as Eq. (10).

$$\rho C_p \frac{\partial \widetilde{T}}{\partial t} - \lambda \left(\frac{1}{r^2}\frac{\partial^2 \widetilde{T}}{\partial \theta^2} + \frac{\partial^2 \widetilde{T}}{\partial z^2} \right) + \frac{2h\widetilde{T}}{e} + r_\varepsilon = w'_{ch} \tag{10}$$

With ρ the density, C_p the specific heat, λ the thermal conductivity, h the coefficient of forced convection with air and r_ε the radiation losses calculated using Stefan Boltzmann's law. Finally $\widetilde{T} = T - T_{amb}$ is the in-test temperature variation, the difference between the current temperature T and the initial temperature T_0 (assumed to be equal to the ambient temperature $T_0 = T_{amb}$).

The last unknown is the volume heat source w'_{ch} (expressed in Watts per cubic meters) and especially its spatial distribution. The heat input within the elements beneath the tool is assessed from the Finite-element models described in "Finite Element Model" section. The heat flux across the top surface denoted q_z is divided by the element thickness dz in order to obtain the corresponding volume power that enters the first line element. In addition, the plasticity-related dissipation underneath the tool is accounted by adding spatial distribution of w'_p stems from the FEM models (see Fig. 11). The obtained input specific power $w'_{ch} = q_z/dz + w'_p$ is assumed to remain constant during the cut and depending only on the cutting parameters such as cutting velocity, feed, rake angle, etc. It is therefore assessed, once and for all, from the FE model that matches the experimental cutting conditions.

Results and discussion

Chip morphology

The chip morphology of a 3 mm deep through drill is depicted in Fig. 12. It is seen that the shape of the generated chip constantly evolves as the drill progresses. First, in Fig. 12a a transition zone is visible while the tool reaches its effective working diameter. Then from 12b–c, the cut seems to reach steady conditions although it is observed that the curvature and frequency of the chip slowly decreases and ends up being significantly different from 12 b–c. Such observation gives clue to a slow but continuous evolution of the cutting conditions. Indeed, since velocities, angles, feed and material can be regarded as constant throughout this period of time it is reasonable to assume that such evolution results from the increasing stresses on the chip (with the progressive engagement of the tool in the part) but also from the variation of the thermal conditions accompanying the cut. These phenomena intensify during the drilling process and cause this particular visible chip morphology presented in Fig. 12d and onward in the chip.

Such observations lead to wonder about the time of setting up of the steady thermal regime if ever to establish. It therefore becomes obvious that studying the drilling process after several turns is highly relevant and hence justify the development of the extended thermal model presented in "Extended thermal model" section.

From a radial standpoint, it can be seen from Fig. 13 that the segmentation behavior of the chip differs according to the location along the cutting edge. For the pin (at and around the center of the drill bit) the chip exhibits a clear serrated shape. For T3 the same behavior is also observed. At these two locations the rake angle is small ([0°;16.3°]) for P and ([16.3°;19.9°]) for T3 respectively (see Fig. 3). For T2 and T1 as the rake angle reaches 27.3° and 30° respectively, the segmentation progressively loses its periodic nature. It exhibits a lower magnitude and finally is completely absent for T1. Two comments can be made from these observations (i) these results are consistent with the results published in [22,23] (serrated chips are more prompt to be generated at low cutting speed and low rake angles) and (ii) the discrepancy of the cutting outputs (chips morphology) bears witness of radically different cutting configurations along the cutting edge. This statement explained the edge discretization approach proposed in the following.

First drill revolution

This section presents the numerical (FEM) and experimental results for the first drill revolution.

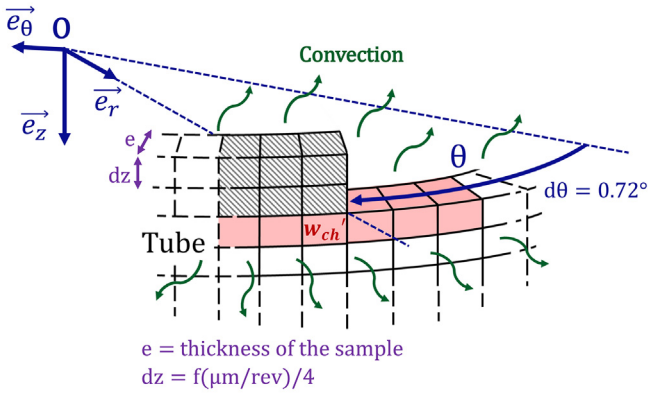


Fig. 11. FDM model.

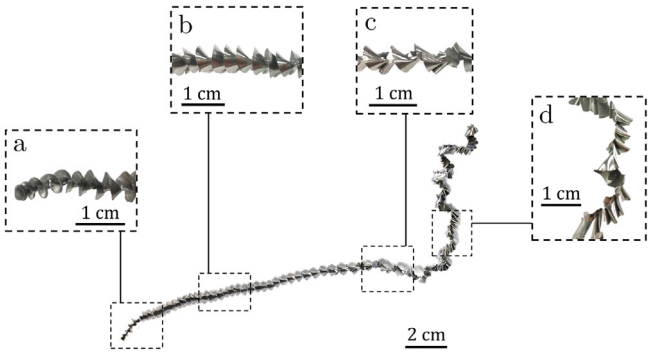


Fig. 12. Photograph of the spiral chip obtained from dry drilling of a block of Ti-6Al-4V.

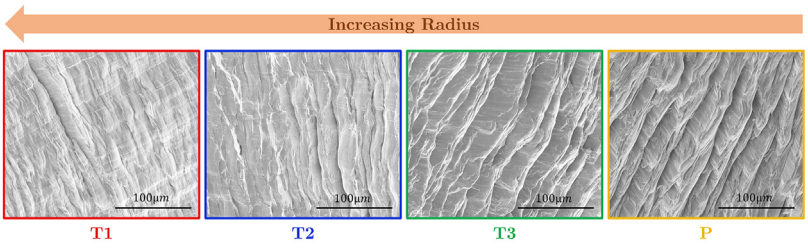


Fig. 13. Top surface SEM images of the chip obtained for the four samples.

Several points should be noticed concerning the comparison of the numerical and experimental fields (see Fig. 15). First of all, repeated passages of chip across the optical path of the camera compromises visibility ahead of the cutting zone. Secondly, the chip quickly moves out of the focus plane and becomes blurry. Consequently, performing DIC within the chip is impossible with such experimental setup. The access to the cutting zone (namely the primary and secondary shear zones) is also made very challenging mainly due to insufficient magnification. Besides, infrared images are motion-blurred in the direct surroundings of the cutting area and in the chip (whose emissivity is also strongly affected by the cut and is mostly unkown – see Fig. 15). Thus, the results within the chip correspond to those acquired with the same emissivity as for the speckled tubes, i.e. 0.88 and are therefore supposed to be highly incorrect. According to such experimental constraints, the present work only focuses on the thermo-mechanical loading arising directly beneath the tool and within the tubes or pin.

Strains

The image correlation technique allows the assessment of the plastic strain from the comparison of two images, prior and after the travel of one tooth of the drill bit at a given location. For the three tubes and the pin, the plastic strains are measured and depicted in Fig. 14. It is observed that the subsurface equivalent plastic strain is higher for the pin than for the other samples; these latter showing a decreasing trend from T3 to T1. It is worth noticing that the feed rate and the edge radius are the same for all tests, thus the explanation for such magnitude discrepancy may either come from the radial cutting speed gradient or the rake angle evolution along the cutting edge. According to Baizeau et al. [4,5] and the angle evolution depicted in Fig. 3, it seems reasonable to assume that the drastic change in rake angle between the Pin ($\gamma_f \approx 0°$) and T1 ($\gamma_f \approx 30°$) is responsible for this result. Here again, and in the light the above, the complex tool geometry clearly leads to significant differences in the cut regime along the cutting edge.

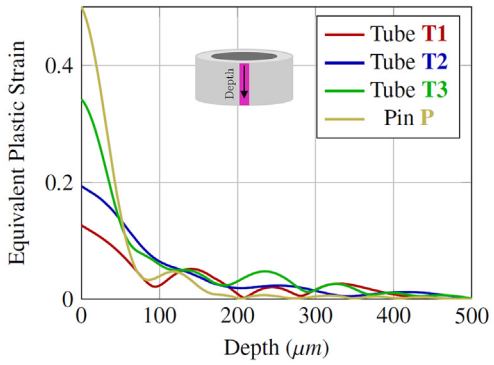


Fig. 14. Experimental equivalent strain values obtained by DIC on the first revolutions on a vertical line beneath the tool.

The depth-wise strain profiles exhibits a rapid decreasing trend. The affected depth extends around 50 µm beneath the surface in all cases (slightly deeper for T2) and becomes negligible after 100 µm. The presence of a burr at the outer periphery of the tubes makes difficult the accurate estimation of the cut surface vertical position. Accordingly, the obtained value of 50 µm must be taken with an uncertainty estimated around ±10 µm from the images. This depth value seems consistent with micro-hardness testing preformed in [34]. However, the radial evolution visible in Fig. 14 was not observed in the work of G. Le Coz et al. though it should be mentioned that the rake angle evolution strongly differs in the two experiments.

Finally, this value of the plasticity affected depth (50 µm) allows to conclude that the heat generation due to subsurface plasticity (see Eq. (8)) becomes negligible below. In addition, this size is close to the metric size of the IR pixel (namely 47.958 µm/pix) which thus enables the assessment of the vertical heat flow from forward finite difference of two successive thermal pixels (see next section).

Thermal results

At first sight, Figs. 15a and b reveal that heat is essentially produced in the primary shear band and consequently instantly drains off with the chip. Nevertheless, these figures also show that the heat diffusing downward, within the samples is far from negligible.

In addition, the numerical results (see Fig. 15a) seem to reveal that heat evacuation in the chip is more important in the case of the pin P than in the case of the tubes T1, T2 and T3. Remember that an emissivity of 0.88 is applied over the whole image, including the chip (where the raw titanium emissivity is very unlikely to exhibit such value), which prevent from any comparison between tests and calculation in this area. However, the first comment allows to assume that the numerical heat diffusing in the workpiece seems to be higher in the case of the tubes than in the case of the pin. This statement is nonetheless not experimentally verified from direct reading of Fig. 15b, especially for the tube T2. However, the temperature strongly depends on various parameters (geometry, boundary conditions, ...) and achieving a relevant confrontation in temperature between tests and calculations is very complex. In particular, the estimation of the peak temperature is highly challenging due to the limited spatial resolution of the experimental means. For this very reason, a power approach, less sensitive to these parameters, is preferred for the study on first revolutions of the drill.

The heat diffusing in the workpiece appears more clearly in Fig. 15c where the vertical heat flow is presented in the numerical case (FEM) and proves to be significant (between 5.10^6 and 12.10^6 W.m^{-2} just under the tool, see Fig. 15d). Both experimental and numerical heat flows are calculated using the Fourier's law. Fluxes are computed from the vertical spatial derivative of the temperature fields using finite difference:

$$\varphi_z = \lambda \frac{dT(\theta, z)}{dz} \tag{11}$$

The same step $\delta_z = 50$ µm, corresponding to the size of one pixel, is used in both experimental and numerical calculation. The heat

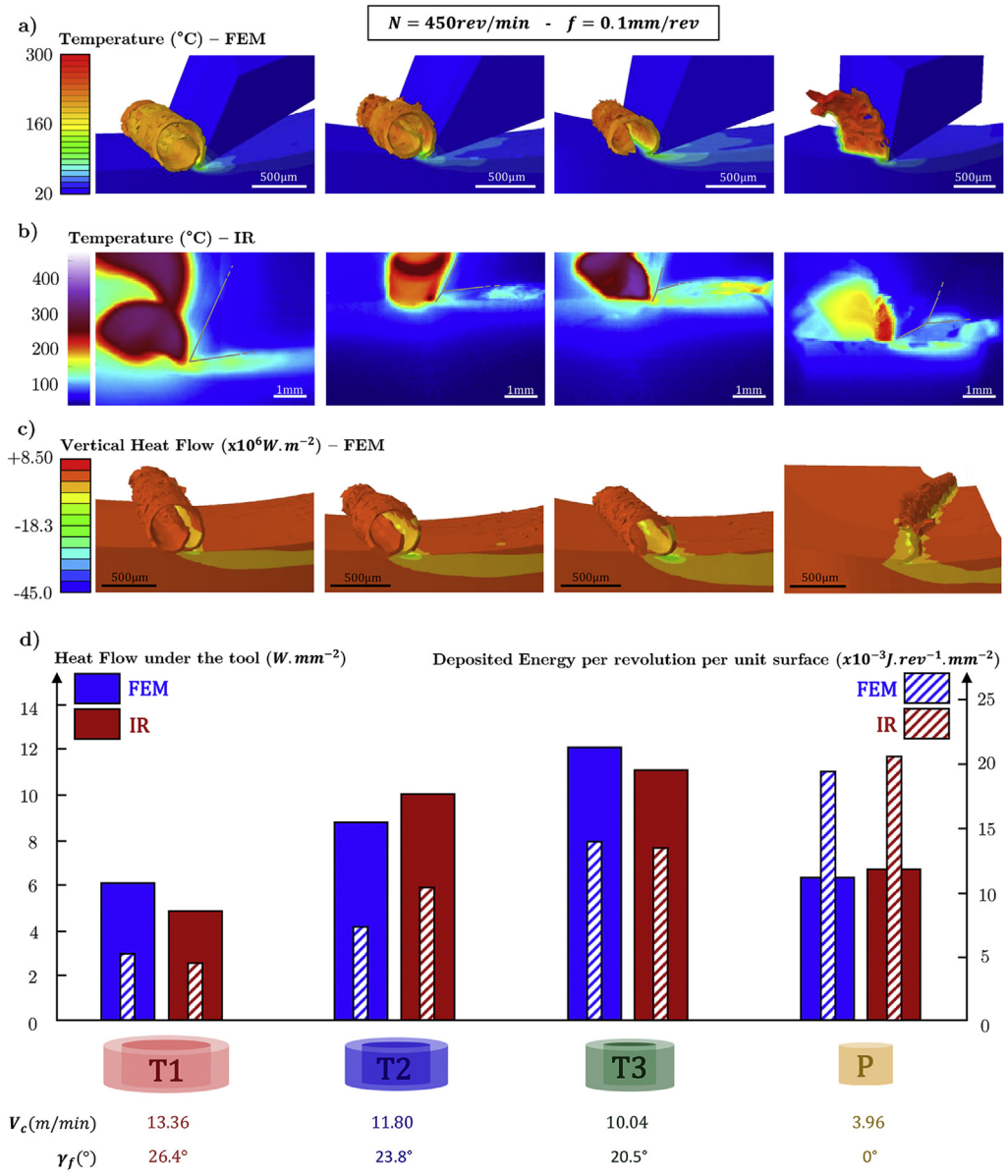


Fig. 15. Thermal results on the 1*st* revolutions for a spindle speed $N = 450$ rev/min and a feed rate $f = 0.1$ mm/rev – (a) FEM Temperature (b) IR Temperature (c) FEM Vertical Heat Flow (d) Heat Flow under the tool and deposited energy per rev per unit of the workpiece surface (50 µm × 50 µm) – for every local cutting speed V_c and local rake angle γ_f.

flows magnitudes obtained right beneath the tool (area of 50 µm × 50 µm) are presented in Fig. 15d). There is a good fit between the heat flow calculated from infrared images and the one obtained by the FE model for the samples T2, T3 and P (respectively differences of 12.5, 8.7 and 5.7% with experiments, see Fig. 15d). The results for the tube T1 are less satisfying (difference of 25.3% with experiments). However, the lower quality of T1 infrared images (slightly out of focus) compromises relevant assessment of the heat flow under the tool.

The heat flux depicted in 15d could seem surprising. Indeed, as recalled in the above, the heat generated beneath the tool has two origins both of which linearly depend on the cutting speed: through the sliding velocity for the friction heat (Eq. (6)) and through the strain-rate for plasticity (Eq. (8)). It is therefore expected that the heat flux developed beneath the tool increases with the effective radius of cut (i.e. from the center toward the outer radius). However, at small rake angle (when getting closer to the center), the stresses involved in metal cutting are known to increase and hence trigger a larger heat extrusion (through the same two equations). These two contradictory behaviours explain the general shape in this plot.

Energies are also depicted in Fig. 15d. They are obtained from the above mentioned fluxes. It corresponds to the amount of energy deposited per unit surface during one revolution. The equation reads:

$$e_z = \frac{1}{S_k}\int_0^{1rev}\iint_S \varphi_z \, dS \, dt \tag{12}$$

Where S_k stands for the total surface that comes in contact with the tool during one revolution (the conical top surface of the sample). It is seen from these overall energy histograms (Fig. 15d) that even if the heat flux is smaller for the pin (mainly because the smaller cutting speed at this location overtakes the stress increase due to the smaller rake angle) it leads to a higher energy deposition

within the material. At this location the one-revolution path of the tool is shorter and thus increases the heat exposure of a given surface unit of the material. In other words, the source has a lower magnitude but remains above a given unit surface for a longer span of time.

This primary thermal comparison, on the first revolutions of the tool, enables to compare FE numerical results with experimental data. It validates the relevance of the numerical heat flow computed by the FE model and proves the reliability of the implemented thermo-mechanical constitutive equations.

Although proven worthy by the above validation considerations, the investigation of the only first revolution fails to answer the central question resulting from the existence of a significant vertical heat flow: what becomes of the heat that enters the tube material? Indeed, it could either lead to a gradual temperature rise in the cutting area as the drill progresses or just being evacuated by the chip when the next tooth passes by. The next section deals with this issue.

After n *drill revolutions*

This section presents the results of the extended numerical model (FEM + FDM) and confronts them with the experimental measurements after several drill revolutions. It is recalled that the power input in the top elements line of the FD model is obtained from the FEM calculation presented in “Thermal results” section.

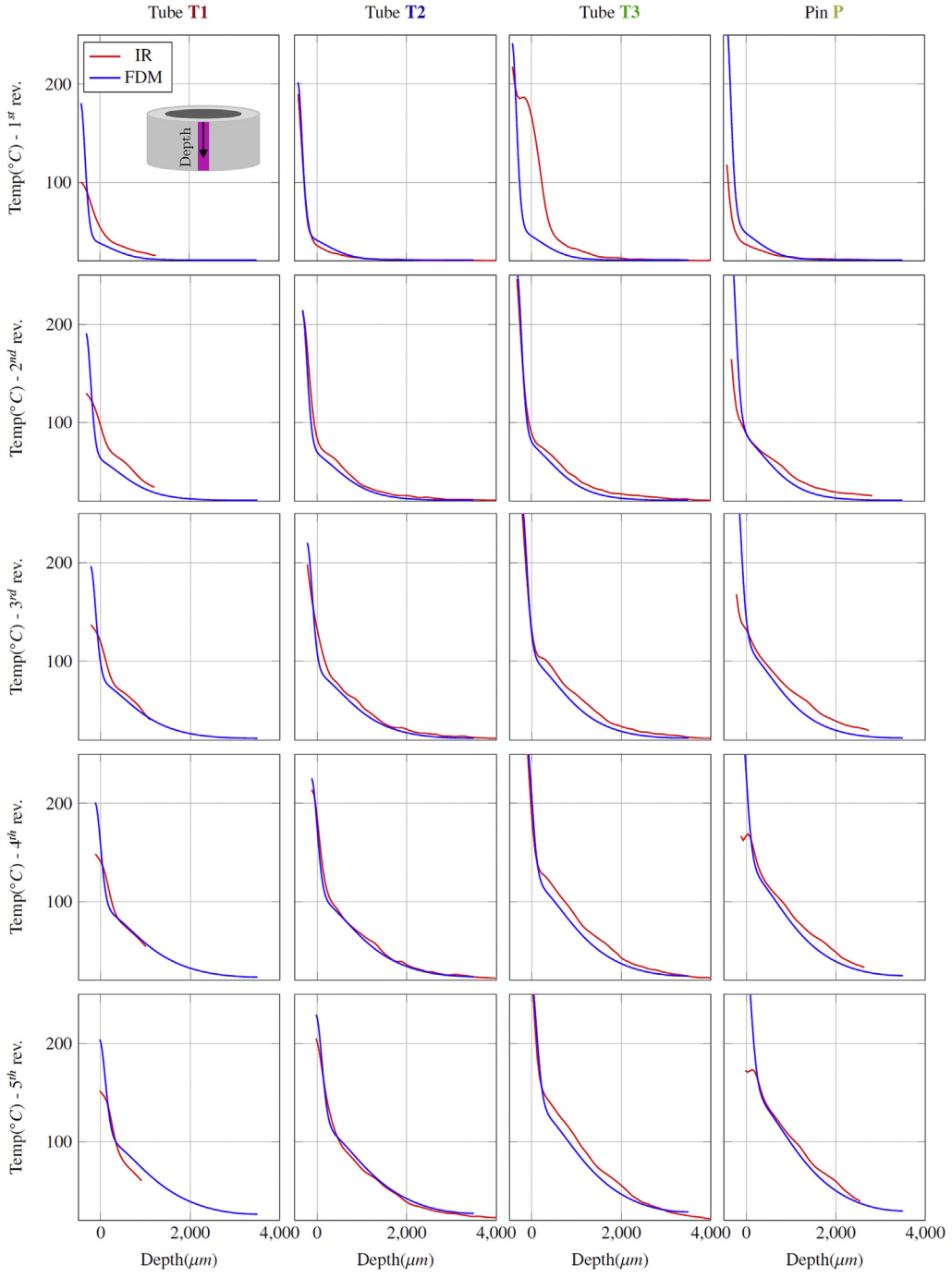


Fig. 16. Numerical (FEM + FDM) and experimental (IR) vertical temperature profiles for an elements column right under the tool for the 4 samples.

This confrontation enables to evaluate the accuracy of the power input and thus the reliability of the thermo-mechanical coupling implemented within the FE model.

Fig. 16 depicts the vertical temperature profiles of the models and the experiments for the three tubes and the pin. First, it is seen that the general shapes of these curves match. Accordingly, it is reasonable to assume that the implementation of both thermal conductivity and boundary conditions is robust. In addition, the areas underneath these curves, which represent the amount of energy that spreads within the work-piece also exhibit a good match.

It is also seen from Fig. 16 that in the close vicinity of the tool, the measurements and models mismatches become significant. Indeed, the maximum temperature (right underneath the tool) seems largely overestimated by he models. This observation results from the discrepancy in spatial resolution of the two approaches. The size of the elements used for the FDM approach is $25^2\,\mu m^2$ while the experimental pixel size is $47.9^2\,\mu m^2$ thus leading to an excessive averaging and an obvious underestimation of a very localize temperature peak from the experimental results. Such experimental approach seems therefore not the most suited to anyone willing to assess the maximum in-process temperature.

A more general comment would be that the temperature is probably not the most interesting output gained from the use of modelling. It strongly depends on the part geometry and the boundary conditions and it is experimentally very challenging to assess its maximum since this latter is located on a free surface. Indeed, the results presented here only intend to validate the genuine data of interest, namely the input power w'_{ch}.

Besides, it is also observed from Fig. 16 that the temperature rapidly builds up within the work-piece as the drill progresses (vertical reading of Fig. 16, more obvious in Fig. 17). It should be recalled that the extended model account for the heat suppression prompt by the chip ejection. In other words, despite the fact that a significant part of the heat deposited by the nth tooth passage is evacuated by the $n+1$th tooth passage, the remaining part spreads downward within the workpiece and leads to a rapid increase of its temperature. It is also observed from the isotherms in Fig. 17 that such heat build-up is more significant close to the center of the drilling bit (P and T3) than at the periphery of it (T2 and T1). Such observations are consistent with the heat flux observed from the FE model for the first revolution (see Fig. 15). This challenges the classical hypothesis of heat being mostly evacuated within the chip. This observation is even strengthen recalling that tubes are drilled in this case. Indeed, it is reasonable to assume that such build-up is to be more severe in a case of a blind or through hole where boundary conditions cannot play a moderation role in the temperature rise. This is clearly visible from Fig. 18, where the increase of the thermal leakage after 5 revolutions tends to stabilize the temperature (even though no clear stall of the temperature is visible after 5 rev.).

Fig. 18 presents the thermal history of a $50\,\mu m \times 50\,\mu m$ fixed zone located $500\,\mu m$ beneath the initial top surface (which becomes the top surface when the drill is completed after 5 rev.). This zone corresponds to one Infrared pixel from the experimental data and two superposed FDM elements from the numerical data. Once again, the extended model properly predicts the thermal history of the zone underneath the drilling bit. Once again the peak temperature is just poorly estimated by the experimental means. The resolution-based considerations proposed in the above can, here again, explain this very phenomenon along with the fact that for some IR images the chip passes in front of the camera. It is seen that, even if the temperature decreases in-between two successive tooth cut, the remaining lead to a significant and continuous increase of the subsurface temperature, i.e. the raw material to be cut by the next tooth. This is more visible from Fig. 19. This figure presents the thermal evolution of the samples, 1 mm beneath the tool (as the tool progresses). Note that in this case the computation have been run over 20 tool revolutions (yet drilling a hole of 2 mm in depth). It is also worth noticing that such extension in time does not exhibit any stabilization of the temperature. Indeed after 20 rev. the temperature at the center overtake 200 °C and keeps rising. It is recalled that the heat sources retrieved from the FE models are computed with an incoming material temperature of 20° thus the validity of the inputs after 20 revolution is questionable since it is widely acknowledge that the mechanical characteristics of Ti-6Al-4V significantly drop in the 300–500 °C temperature range [28].

Such heat accumulation within the cut material inevitability leads to a subsequent heat build-up within the tool from thermal

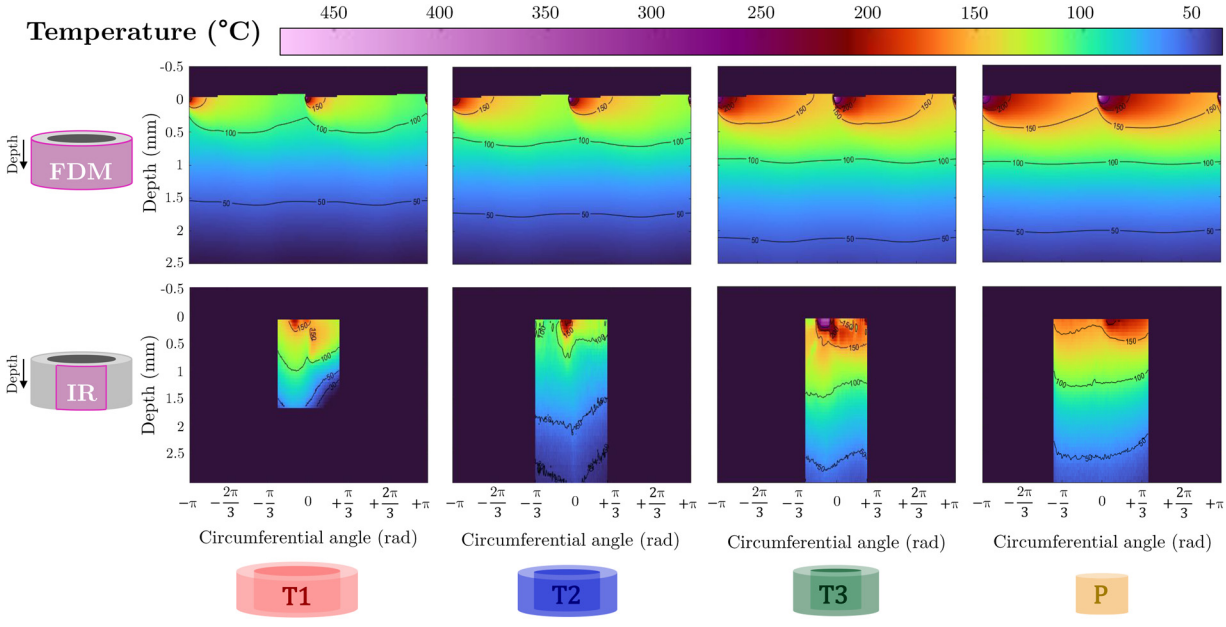


Fig. 17. Numerical (FEM + FDM) and Experimental (IR) thermal fields obtained on the flattened external surfaces of each sample after 5 drill revolutions.

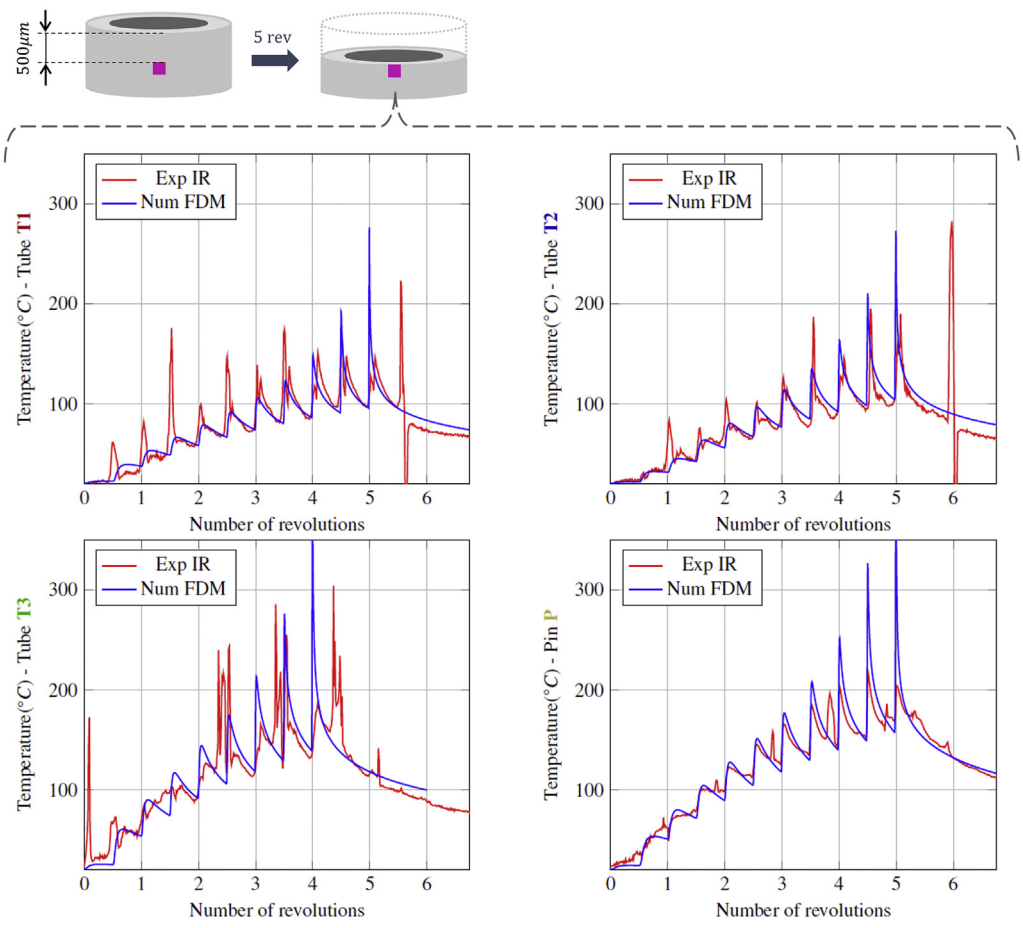


Fig. 18. Numerical (FEM + FDM) and Experimental (IR) thermal history of a point initially located 500 μm beneath the top surface (and that utlimately comes in contact with the tool).

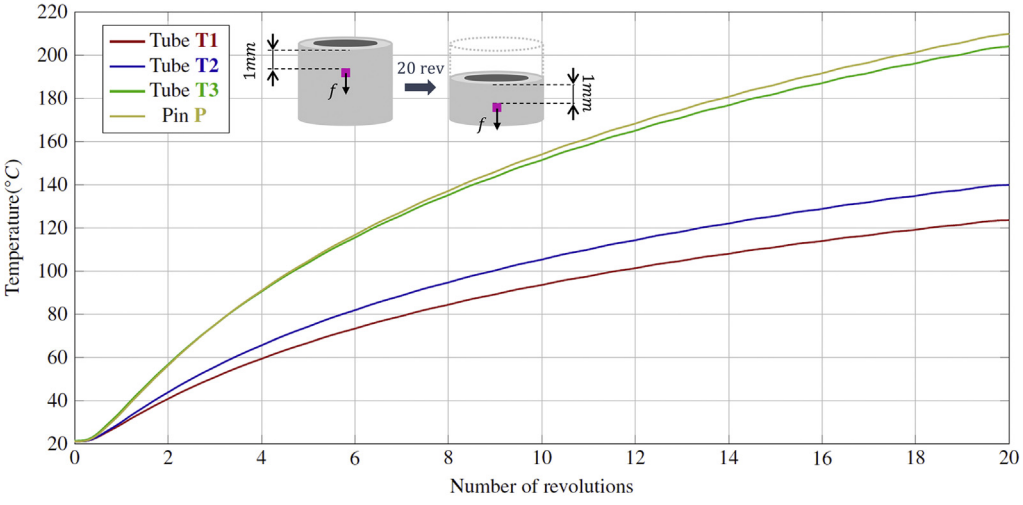


Fig. 19. Numerical (FEM + FDM) temperature after 20 revolutions – moving zone 1 mm under the tool.

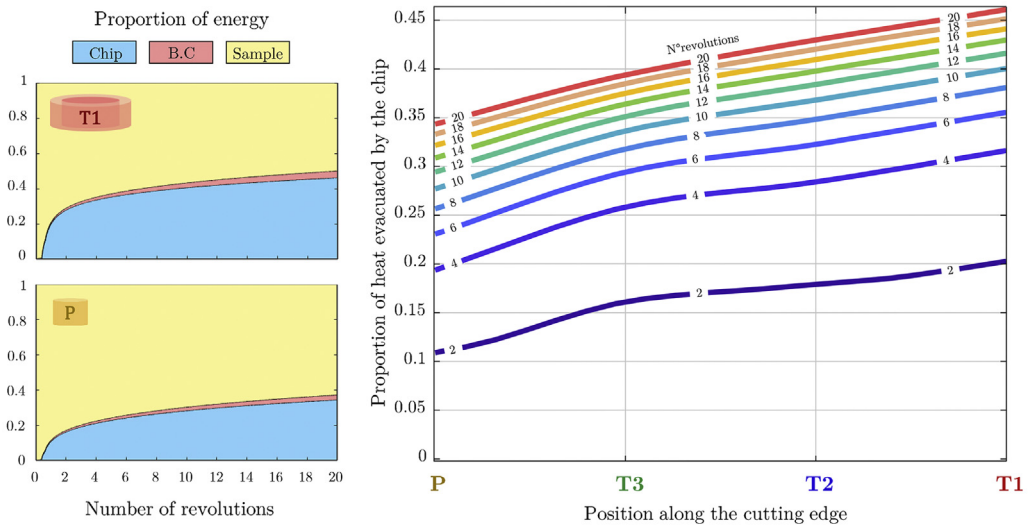


Fig. 20. Numerical prediction of the energy budget (a) time evolution of the part of energy that enters the material and that ultimately remain in it (yellow), is drains off latter by the chip (blue), and lost to the environment (red) – (b) Radius wise representation of the energy budget (time evolution).

contact. Such mechanism can be identified as one of the causes behind the cut instability observed from post-mortem chip micrographies (depicted in Fig. 12) and also possibly as a contributing factor the tool damage.

It is also observed from Figs. 17–19 that the amount of heat deposited within the material differs from one tube to another. Indeed two zones along the cutting edge radius R can be singled out:

Zone 1 comprises $R \in [0\,;0.65R_{max}]$ corresponding to T2 and T3. Two competing factors lead to a high heat deposition. In P, the input power is lower (see Fig. 15d) but is spread over a small surface (smaller circumference). In T3, the circumference increases significantly but the input power is higher. Consequently for these two specimens the temperature rises significantly higher than for the outer periphery of the drill bit.

Zone 2 comprises $R \in [0.65R_{max}\,;R_{max}]$ corresponding to T2 and T1. In this zone, the continuous decrease of the input flux along with the increase in the circumference (and yet the surface over which the heat input is spread) leads to a smaller thermal build up.

Another explanation for this observation could be that the amount of the heat deposited at revolution n and removed at revolution $n+1$ is different at the center and at the periphery of the drilling bit. Thanks to the extended FD model this information is also available for each sample. Fig. 20 shows the ultimate destination of the heat that enters the tube/pin material. It is observed, after 20 revolutions, that between 34% and 46% of the heat that enters the material ultimately ends up being evacuated withing the chip (that sums up with the heat already generated withing the chip from plasticity in the primary shear zone). It is also observed that this ratio slightly increases from the center to the periphery of the drill bit. However this increase is clearly not sufficient to explain, alone, the observed differences of temperatures in Zone no.1 and no.2. Hence, the above mentioned observations on the spread surface still holds and seems to be the major contributor to the radial temperature gradient.

Finally, It is also seen from the comparison of Figs. 20 and 19, that the amount of heat transferred to the material and ultimately retrieved within the chip is correlated to the material temperature. As the temperature curve tends to flatten, so does the amount of heat evacuated by the chip. Consequently, under the given cutting conditions (speed and feed rate), the temperature under the tool cannot decrease if not for the action of the boundary conditions. In other words, the thermal heat front wave moves downward faster than the tool. The introduction of cutting fluid in the model would be interesting and could limit this temperature increase under the tool. However, the introduction of fluid/structure interaction would considerably impair the computation time. Besides, in order to compare the results, other experimental setups should be investigated.

Conclusion

The paper proposes a complete numerical chain that allows the estimation of various thermal related variables associated with hole drilling in Ti-6Al-4V alloy. It aims at tackle a reputedly complex issue, and do not offer a straight forward and easy way to access thermal information. It rather proposes a multi-scale modelling based on local information obtained by a mixed numerical/experimental approach.

- The proposed method offers a new insight on the in-process thermal events occurring along the cutting edge and within the material bulk beneath it. Indeed, the complexity of the thermal scene and the amount of contributing factor to it, turn the understanding of drilling mechanisms into a (sometime counter-intuitive) challenge.
- The contribution of local (small scale) information is proven worthy in strengthening and validating macroscopic models that bring relevant knowledge on the energy budget of the drill operation.
- It has been shown that the variation of cutting speed and rake angle along the cutting edge is responsible for significant radial evolution of the thermo-mechanical loading. This observation strengthens the relevance of the edge discretization approaches.
- In addition, it has been shown that even for a reasonably small feed-rate (0.1 mm/rev), the thermal build up within the material bulk is far from negligible and reaches a first critical temperature for Ti-6Al-4V mechanical behaviour at a very short horizon (200 °C after 1.8 mm of drill in the present configuration).
- This study confirms that the heat is mostly evacuated by the chip (mainly from primary and secondary shear zone) but such hypothesis does not prevent from paying attention to the bulk material temperature rise as the tool progresses.

- It is also shown that part of the energy entering the material ultimately ends up being ejected by the chip and preliminary results show that this ratio is significantly affected by the cutting parameters (cutting speed and feed) but also depends on the tool geometry (rake angle variations along the cutting edge).
- The main drawbacks rely firstly on the use of heavy Finite Element modeling that needs to be run for every cutting configuration (cutting speed, feed, etc.).
- A second drawback lies on the absence of investigation on the holes wall thermo-mechanical loading (and the peripheral edge influence).

Such conclusions open interesting perspectives in using numerical models to investigate the thermal aspects of the drilling operation. Further work will focus on optimizing the cutting parameters in order to minimize the temperature rise within the material. In addition, the proposed approach can also prove worthy in the assessment of the Taylor Quinney coefficient for the sensitivity of the thermal output to this parameter is here highlighted.

Finally, this work is part of a larger study. Indeed, the complete pin drilling of Ti-6Al-4V is also studied with the same tool and the same cutting conditions. Thus, a future work that aims at comparing the results obtained during the complete pin drilling with these present results is to be addressed.

Declaration of interests

The authors declare that they have no known competing financial interests or personal relationships that could have appeared to influence the work reported in this paper.

Acknowledgement

The authors would like to thank the region Occitanie for its financial support. This work was carried out within the context of the working group Manufacturing'21 which gathers 21 French research laboratories. The topics approached are: modelling of the manufacturing processes, virtual machining, and emergence of new manufacturing methods.

References

[1] Abaqus documentation.http://130.149.89.49:2080/v2016/index.html.
[2] Matlab documentation.https://www.mathworks.com/help/matlab/.
[3] Arif, R., Fromentin, G., Rossi, F., Marcon, B., 2019, Mechanical analysis of local cutting forces and transient state when drilling of heat-resistant austenitic stainless steel. Int J Adv Manuf Technol, 104/5–8: 2247–2258. http://dx.doi.org/10.1007/s00170-019-03969-8.
[4] Baizeau, T., Campocasso, S., Fromentin, G., Rossi, F., Poulachon, G., 2015, Effect of rake angle on strain field during orthogonal cutting of hardened steel with c-BN tools. Proc CIRP, 31:166–171. http://dx.doi.org/10.1016/j.procir.2015.03.089.
[5] Baizeau, T., Campocasso, S., Fromentin, G., Besnard, R., 2017, Kinematic field measurements during orthogonal cutting tests via DIC with double-frame camera and pulsed laser lighting. Exp Mech, 57/4: 581–591. http://dx.doi.org/10.1007/s11340-016-0248-9.
[6] Beno, T., Hulling, U., 2012, Measurement of cutting edge temperature in drilling. Proc CIRP, 3:531–536. http://dx.doi.org/10.1016/j.procir.2012.07.091.
[7] Brynk, T., Romelczyk-Baishya, B., 2018, Residual stress estimation based on 3D DIC displacement filed measurement around drilled holes. Proc Struct Integr, 13:1267–1272. http://dx.doi.org/10.1016/j.prostr.2018.12.259.
[8] Calamaz, M., Limido, J., Nouari, M., Espinosa, C., Coupard, D., Salaün, M., et al, 2009, Toward a better understanding of tool wear effect through a comparison between experiments and SPH numerical modelling of machining hard materials. Int J Refract Metals Hard Mater, 27/3: 595–604. http://dx.doi.org/10.1016/j.ijrmhm.2008.09.005.
[9] Cantero, J., Tardío, M., Canteli, J., Marcos, M., Miguélez, M., 2005, Dry drilling of alloy Ti-6Al-4V. Int J Mach Tools Manuf, 45/11: 1246–1255. http://dx.doi.org/10.1016/j.ijmachtools.2005.01.010.
[10] Chrysochoos, A., Louche, H., 2000, An infrared image processing to analyze the calorific effects accompanying strain localisation. Int J Eng Sci, 38/16: 1759–1788. http://dx.doi.org/10.1016/S0020-7225(00)00002-1.
[11] Courbon, C., Mabrouki, T., Rech, J., Mazuyer, D., D'Eramo, E., 2013, On the existence of a thermal contact resistance at the tool-chip interface in dry cutting of AISI 1045: formation mechanisms and influence on the cutting process. Appl Therm Eng, 50/1: 1311–1325. http://dx.doi.org/10.1016/j.applthermaleng.2012.06.047.
[12] Courbon, C., Mabrouki, T., Rech, J., Mazuyer, D., Perrard, F., D'Eramo, E., 2014, Further insight into the chip formation of ferritic-pearlitic steels: Microstructural evolutions and associated thermo-mechanical loadings. Int J Mach Tools Manuf, 77:34–46. http://dx.doi.org/10.1016/j.ijmachtools.2013.10.010.
[13] Cuesta, M., Aristimuño, P., Garay, A., Arrazola, P., 2016, Heat transferred to the workpiece based on temperature measurements by IR technique in dry and lubricated drilling of Inconel 718. Appl Therm Eng, 104:309–318. http://dx.doi.org/10.1016/j.applthermaleng.2016.05.040.
[14] Díaz-Álvarez, J., De-La-Cruz-Hernández, J., Díaz-Álvarez, A., Cantero-Guisández, J., 2015, Numerical modelling of the thermal effects on material in drilling processes Ti6Al4V alloy. Proc Eng, 132:427–432. http://dx.doi.org/10.1016/j.proeng.2015.12.515.
[15] Fernandes, M., Fonseca, E., Natal, R., 2016, Thermal analysis during bone drilling using rigid polyurethane foams: numerical and experimental methodologies. J Braz Soc Mech Sci Eng, 38/7: 1855–1863. http://dx.doi.org/10.1007/s40430-016-0560-4.
[16] Fernandes, M., Fonseca, E., Jorge, R., 2019, Thermo-mechanical stresses distribution on bone drilling: numerical and experimental procedures. Proc Inst Mech Eng Part L J Mater Des Appl, 233/4: 637–646. http://dx.doi.org/10.1177/1464420716689337.
[17] Ginting, A., Nouari, M., 2009, Surface integrity of dry machined titanium alloys. Int J Mach Tools Manuf, 49/3-4: 325–332. http://dx.doi.org/10.1016/j.ijmachtools.2008.10.011.
[18] Girinon, M., Valiorgue, F., Rech, J., Feulvarch, É., 2016, Development of a procedure to characterize residual stresses induced by drilling. Proc CIRP, 45:79–82. http://dx.doi.org/10.1016/j.procir.2016.02.074.
[19] Girinon, M., Valiorgue, F., Karaouni, H., Feulvarch, É., 2018, 3D numerical simulation of drilling residual stresses. C R Mec, 346:701–711. http://dx.doi.org/10.1016/j.crme.2018.06.003.
[20] Gnanamanickam, E., Lee, S., Sullivan, J., Chandrasekar, S., 2009, Direct measurement of large-strain deformation fields by particle tracking. Meas Sci Technol, 20/9. http://dx.doi.org/10.1088/0957-0233/20/9/095710.
[21] Han, S., Faverjon, P., Valiorgue, F., Rech, J., 2017, Heat flux density distribution differences in four machining processes of AlSi7 block: MQL drilling, tapping, reaming and dry milling. Proc CIRP, 58:61–66. http://dx.doi.org/10.1016/j.procir.2017.03.196.
[22] Harzallah, M., Pottier, T., Senatore, J., Mousseigne, M., Germain, G., Landon, Y., 2017, Numerical and experimental investigations of Ti-6Al-4V chip generation and thermo-mechanical couplings in orthogonal cutting. Int J Mech Sci, 134:189–202. http://dx.doi.org/10.1016/j.ijmecsci.2017.10.017.
[23] Harzallah, M., Pottier, T., Gilblas, R., Landon, Y., Mousseigne, M., Senatore, J., 2018, A coupled in-situ measurement of temperature and kinematic fields in Ti-6Al-4V serrated chip formation at micro-scale. Int J Mach Tools Manuf, 130–131:20–35. http://dx.doi.org/10.1016/j.ijmachtools.2018.03.003.
[24] Hussein, R., Sadek, A., Elbestawi, M., Attia, M., 2020, Effect of process parameters on chip formation during vibration-assisted drilling of Ti6Al4V. Int J Adv Manuf Technol, 106:1105–1119. http://dx.doi.org/10.1007/s00170-019-04627-9.
[25] Imbrogno, S., Sartori, S., Bordin, A., Bruschi, S., Umbrello, D., 2017, Machining simulation of Ti6Al4V under dry and cryogenic conditions. Proc CIRP, 58:475–480. http://dx.doi.org/10.1016/j.procir.2017.03.263.
[26] Isobe, H., Uehara, Y., Hara, K., 2012, Effect of ultrasonic vibration drilling on cutting stress distribution. Key Eng Mater, 523–524:191–196. http://dx.doi.org/10.4028/www.scientific.net/KEM.523-524.191.
[27] Johnson, G., Cook, W., 1983, A constitutive model and data for metals subjected to large strains, high strain rates and high temperatures. Proceedings of the seventh international symposium on ballistics 21, 541–547.
[28] Komanduri, R., Hou, Z.-B., 2002, On thermoplastic shear instability in the machining of a titanium alloy (Ti-6Al-4V). Metall Mater Trans A, 33:2995–3010. http://dx.doi.org/10.1007/s11661-002-0284-1.
[29] Kumar, A., Bhardwaj, R., Joshi, S., 2020, Thermal modeling of drilling process in titanium alloy (Ti-6Al-4V). Mach Sci Technol, 24/3: 341–365. http://dx.doi.org/10.1080/10910344.2019.1698607.
[30] Lacombe, A., Landon, Y., Paredes, M., Chirol, C., Benaben, A., 2020, Impact of the hole surface integrity on the fatigue life of a 2024-T351 aluminium drilled part. Authorea, . http://dx.doi.org/10.22541/au.160071421.14927969.
[31] Lane, B., Whitenton, E., Madhavan, V., Donmez, A., 2013, Uncertainty of temperature measurements by infrared thermography for metal cutting applications. Metrologia, 50:637–653. http://dx.doi.org/10.1088/0026-1394/50/6/637.
[32] Lazoglu, I., Poulachon, G., Ramirez, C., Akmal, M., Marcon, B., Rossi, F., et al, 2017, Thermal analysis in Ti-6Al-4V drilling. CIRP Ann – Manuf Technol, 66/1:105–108. http://dx.doi.org/10.1016/j.cirp.2017.04.020.
[33] Le Coz, G., Marinescu, M., Devillez, A., Dudzinski, D., Velnom, L., 2012, Measuring temperature of rotating cutting tools: application to MQL drilling and dry milling of aerospace alloys. Appl Therm Eng, 36:434–441. http://dx.doi.org/10.1016/j.applthermaleng.2011.10.060.
[34] Le Coz, G., Jrad, M., Laheurte, P., Dudzinski, D., 2017, Analysis of local cutting edge geometry on temperature distribution and surface integrity when dry drilling of aeronautical alloys. Int J Adv Manuf Technol, 93/5–8: 2037–2044. http://dx.doi.org/10.1007/s00170-017-0671-9.

[35] Li, J., Tao, Z., Cai, X., An, Q., Chen, M., 2020, Experimental and finite element analysis of the formation mechanism of serrated chips of nickel-based superalloy Inconel 718. Int J Adv Manuf Technol, 107:4969–4982. http://dx.doi.org/10.1007/s00170-020-05150-y.

[36] Mabrouki, T., Girardin, F., Asad, M., Rigal, J., 2008, Numerical and experimental study of dry cutting for an aeronautic aluminium alloy (A2024-T351). Int J Mach Tools Manuf, 48/11: 1187–1197. http://dx.doi.org/10.1016/j.ijmachtools.2008.03.013.

[37] Mathew, N., Laxmanan, V., 2018, Temperature rise in workpiece and cutting tool during drilling of titanium aluminide under sustainable environment. Mater Manuf Process, 33/16: 1765–1774. http://dx.doi.org/10.1080/10426914.2018.1476770.

[38] Novovic, D., Dewes, R., Aspinwall, D., Voice, W., Bowen, P., 2004, The effect of machined topography and integrity on fatigue life. Int J Mach Tools Manuf, 44:125–134. http://dx.doi.org/10.1016/j.ijmachtools.2003.10.018.

[39] Pan, B., Lu, Z., Xie, H., 2010, Mean intensity gradient: an effective global parameter for quality assessment of the speckle patterns used in digital image correlation. Optics Lasers Eng, 48/4: 469–477. http://dx.doi.org/10.1016/j.optlaseng.2009.08.010.

[40] Pecat, O., Brinksmeier, E., 2014, Low damage drilling of CFRP/titanium compound materials for fastening. Proc CIRP, 13:1–7. http://dx.doi.org/10.1016/j.procir.2014.04.001.

[41] Pottier, T., Germain, G., Calamaz, M., Morel, A., Coupard, D., 2014, Sub-millimeter measurement of finite strains at cutting tool tip vicinity. Exp Mech, 54/6: 1031–1042. http://dx.doi.org/10.1007/s11340-014-9868-0.

[42] Poutord, A., Rossi, F., Poulachon, G., M'Saoubi, R., Abrivard, G., 2016, Study of the local forces along a cutting edge when drilling Ti6Al4V – comparison of methods. Int J Mach Mach Mater, 18/5–6: 621–633. http://dx.doi.org/10.1504/IJMMM.2016.078976.

[43] Pujana, J., Arrazola, P., Villar, J., 2008, In-process high-speed photography applied to orthogonal turning. J Mater Process Technol, 202/1–3: 475–485. http://dx.doi.org/10.1016/j.jmatprotec.2007.10.007.

[44] Rech, J., Arrazola, P., Claudin, C., Courbon, C., Pusavec, F., Kopac, J., 2013, Characterisation of friction and heat partition coefficients at the tool-work material interface in cutting. CIRP Ann – Manuf Technol, 62/1: 79–82. http://dx.doi.org/10.1016/j.cirp.2013.03.099.

[45] Rittel, D., 1999, On the conversion of plastic work to heat during high strain rate deformation of glassy polymers. Mech Mater, 31/2: 131–139. http://dx.doi.org/10.1016/S0167-6636(98)00063-5.

[46] Rittel, D., Zhang, L., Osovski, S., 2017, The dependence of the Taylor-Quinney coefficient on the dynamic loading mode. J Mech Phys Solids, 107:96–114. http://dx.doi.org/10.1016/j.jmps.2017.06.016.

[47] Samy, G., Kumaran, S.T., 2017, Measurement and analysis of temperature, thrust force and surface roughness in drilling of AA (6351)-B4C composite. Meas: J Int Meas Confed, 103:1–9. http://dx.doi.org/10.1016/j.measurement.2017.02.016.

[48] Sato, M., Aoki, T., Tanaka, H., Takeda, S., 2013, Variation of temperature at the bottom surface of a hole during drilling and its effect on tool wear. Int J Mach Tools Manuf, 68:40–47. http://dx.doi.org/10.1016/j.ijmachtools.2013.01.007.

[49] Schreier, H., Orteu, J.-J., Sutton, M.A., 2009, Image correlation for shape, motion and deformation measurements. Springer. http://dx.doi.org/10.1007/978-0-387-78747-3.

[50] Slim, B.M., 2011, Modélisation hybride du frottement local à l'interface outil-copeau en usinage des alliages métalliques. École Nationale Supérieure d'Arts et Métiers. PhD Thesis.

[51] Taskesen, A., Kutukde, K., 2015, Non-contact measurement and multi-objective analysis of drilling temperature when drilling B4C reinforced aluminum composites. Trans Nonferrous Metals Soc China (Engl Ed), 25/1: 271–283. http://dx.doi.org/10.1016/S1003-6326(15)63602-0.

[52] Taylor, G., Quinney, H., 1934, The latent energy remaining in a metal after cold working. Proc R Soc Lond, 143/849: 307–326. http://dx.doi.org/10.1098/rspa.1934.0004.

[53] Ueda, T., Nozaki, R., Hosokawa, A., 2007, Temperature measurement of cutting edge in drilling – effect of oil mist-. CIRP Ann – Manuf Technol, 56/1: 93–96. http://dx.doi.org/10.1016/j.cirp.2007.05.024.

[54] Valiorgue, F., Rech, J., Hamdi, H., Gilles, P., Bergheau, J., 2012, 3D modeling of residual stresses induced in finish turning of an AISI304L stainless steel. Int J Mach Tools Manuf, 53:77–90. http://dx.doi.org/10.1016/j.ijmachtools.2011.09.011.

[55] Whittam, A., Simpson, R., McEvoy, H., 2014, Performance tests of thermal imaging systems to assess their suitability for quantitative temperature measurement. 12th international conference on quantitative infrared thermography, . http://dx.doi.org/10.21611/qirt.2014.202.

[56] Xu, J., Li, C., Chen, M., El Mansori, M., Paulo Davim, J., 2020, On the analysis of temperatures, surface morphologies and tool wear in drilling CFRP/Ti6Al4V stacks under different cutting sequence strategies. Compos Struct, 234/January 2019: 111708. http://dx.doi.org/10.1016/j.compstruct.2019.111708.

[57] Yadav, S., Saldana, C., Murthy, T., 2015, Deformation field evolution in indentation of a porous brittle solid. Int J Solids Struct, 66:35–45. http://dx.doi.org/10.1016/j.ijsolstr.2015.04.009.

[58] Yang, D., Liu, Z., 2018, Surface integrity generated with peripheral milling and the effect on low-cycle fatigue performance of aeronautic titanium alloy Ti-6Al-4V. Aeronaut J, 122/1248: 316–332. http://dx.doi.org/10.1017/aer.2017.136.

[59] Yang, H., Ding, W., Chen, Y., Laporte, S., Xu, J., Fu, Y., 2019, Drilling force model for forced low frequency vibration assisted drilling of Ti-6Al-4V titanium alloy. Int J Mach Tools Manuf, 146:103438. http://dx.doi.org/10.1016/j.ijmachtools.2019.103438.

[60] Yoon, H., Allen, D., Saunders, R., 2005, Methods to reduce the size-of-source effect in radiometers. Metrologia, 42/2: 89–96. http://dx.doi.org/10.1088/0026-1394/42/2/003.

[61] SECO (SD203A-11.0-33-12R1-M) - Full specification (Accessed May 2021).